AN ULTRA-DEEP NEAR-INFRARED SPECTRUM OF A COMPACT QUIESCENT GALAXY AT $z = 2.2$

MARISKA KRIEK[1], PIETER G. VAN DOKKUM[2], IVO LABBÉ[3], MARIJN FRANX[4], GARTH D. ILLINGWORTH[5],
DANILO MARCHESINI[2], AND RYAN F. QUADRI[4]
[1] Department of Astrophysical Sciences, Princeton University, Princeton, NJ 08544, USA; mariska@astro.princeton.edu
[2] Department of Astronomy, Yale University, New Haven, CT 06520, USA
[3] Hubble Fellow, Carnegie Observatories, Pasadena, CA 91101, USA
[4] Leiden Observatory, Leiden University, NL-2300 RA Leiden, Netherlands
[5] UCO/Lick Observatory, University of California, Santa Cruz, CA 95064, USA

ABSTRACT

Several recent studies have shown that about half of the massive galaxies at $z \sim 2$ are in a quiescent phase. Moreover, these galaxies are commonly found to be ultra-compact with half-light radii of ~ 1 kpc. We have obtained a ~ 29 hr spectrum of a typical quiescent, ultra-dense galaxy at $z = 2.1865$ with the Gemini Near-Infrared Spectrograph. The spectrum exhibits a strong optical break and several absorption features, which have not previously been detected in $z > 2$ quiescent galaxies. Comparison of the spectral energy distribution with stellar population synthesis models implies a low star formation rate (SFR) of 1–3 $M_{\odot}$ yr^{-1}, an age of 1.3–2.2 Gyr, and a stellar mass of $\sim 2 \times 10^{11}$ $M_{\odot}$. We detect several faint emission lines, with emission-line ratios of [N II]/Hα, [S II]/Hα, and [O II]/[O III] typical of low-ionization nuclear emission-line regions. Thus, neither the stellar continuum nor the nebular emission implies active star formation. The current SFR is $< 1\%$ of the past average SFR. If this galaxy is representative of compact quiescent galaxies beyond $z = 2$, it implies that quenching of star formation is extremely efficient and also indicates that low luminosity active galactic nuclei (AGNs) could be common in these objects. Nuclear emission is a potential concern for the size measurement. However, we show that the AGN contributes $\lesssim 8\%$ to the rest-frame optical emission. A possible post-starburst population may affect size measurements more strongly; although a 0.5 Gyr old stellar population can make up $\lesssim 10\%$ of the total stellar mass, it could account for up to $\sim 40\%$ of the optical light. Nevertheless, this spectrum shows that this compact galaxy is dominated by an evolved stellar population.

Key words: galaxies: evolution – galaxies: formation – galaxies: high-redshift

Online-only material: color figures

1. INTRODUCTION

The first massive, quiescent galaxies ($> 10^{11}$ $M_{\odot}$) arose when the universe was only ~ 3 Gyr old (e.g., Labbé et al. 2005; Kriek et al. 2006b; Williams et al. 2008) or perhaps even earlier (e.g., Brammer & van Dokkum 2007; Mancini et al. 2009; Fontana et al. 2009; Mobasher et al. 2005; Wiklind et al. 2008). Remarkably, these galaxies already form a red sequence at $z \sim 2.3$ (Kriek et al. 2008a). The relatively young ages (~ 0.5 Gyr) and post-starburst spectral shapes (Kriek et al. 2006b, 2008a) of the $z \sim 2.3$ red-sequence galaxies suggest that a significant fraction of the stars have formed over a short timescale in an intense starburst. Submillimeter bright galaxies are possible candidates to represent this vigorous phase of star formation (e.g., Chapman et al. 2004; Tacconi et al. 2008; Wall et al. 2008). These dusty starburst galaxies have observed star formation rates (SFRs) of several hundreds up to a thousand solar masses a year. The exact mechanism responsible for transforming such active systems into quiescent galaxies is still subject to debate (e.g., Croton et al. 2006; Bower et al. 2006; Naab et al. 2007; Dekel & Birnboim 2008; Hopkins et al. 2008).

Not all local early types were already massive, quiescent systems at these epochs (e.g., van Dokkum et al. 2006; Taylor et al. 2009a). The majority of them quench or assemble into more massive systems at later times, and the number density of the massive end of the red sequence at $z \sim 2.3$ is only $\sim 1/8$ of the local value (Kriek et al. 2008a). Furthermore, the future evolution of massive quiescent galaxies at $z \sim 2.3$ is still unclear. Their evolved stellar populations suggest that they

passively evolve into their local analogs. However, their strong size and slow color evolution contradict this picture. Recent morphological studies show that massive quiescent systems at $z \sim 2$ are remarkably compact with effective radii of ~ 1 kpc (e.g., Trujillo et al. 2006, 2007; Zirm et al. 2007; Toft et al. 2007; Longhetti et al. 2007; van Dokkum et al. 2008; Cimatti et al. 2008; Franx et al. 2008; Damjanov et al. 2009; van der Wel et al. 2008; Saracco et al. 2009). Local early types of similar stellar mass are about a factor of 5 larger (e.g., van Dokkum et al. 2008). Thus, these high-redshift galaxies must evolve significantly after $z \sim 2$, probably by inside-out growth, primarily through minor mergers (e.g., Bezanson et al. 2009; Naab et al. 2009; van der Wel et al. 2009; Hopkins et al. 2009a). In addition, the slow color evolution of the red sequence from $z \sim 2.3$ to the present implies that passive evolution alone cannot explain the observed color–redshift relation (Kriek et al. 2008a).

However, both the size and color evolution studies are hampered by many uncertainties and detailed, crucial information on the early phases of massive, early type galaxies is still lacking. The constraints on the stellar populations and SFRs at high redshifts are poor, even for galaxies with spectroscopy and mid-infrared photometry (e.g., Kriek et al. 2008b; Muzzin et al. 2009). Thus, it is still unclear how "dead" $z > 2$ quiescent galaxies really are. Also, there are no dynamical mass measurements available for quiescent galaxies beyond $z = 2$. Consequently, all stellar mass estimates are photometric, and thus suffer from uncertainties in the derived stellar populations and from assumptions in the metallicity and the initial mass function (IMF). Moreover, spectroscopic redshifts are extremely difficult to obtain for quiescent galaxies without emission lines. Using
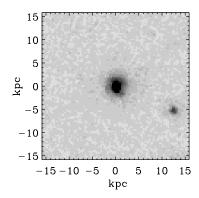
Figure 1. NICMOS image of 1255-0. This image is $3''.8$ by $3''.8$; thus $1''$ corresponds to 8.3 kpc. See van Dokkum et al. (2008) for detailed information and for the images of a large sample of such compact quiescent galaxies at $z \sim 2.3$. The galaxy is barely resolved; most of the visible structure is due to the point-spread function.

Figure 2. Comparison of the broadband photometric rest-frame UV-NIR SED of 1255-0 (black open squares) with the full galaxy sample (colored circles) from MUSYC (Quadri et al. 2007; Marchesini et al. 2009). To match the redshift and stellar mass of 1255-0, we restrict the sample to galaxies in the range $1.9 < z_{phot} < 2.5$ and $11.0 < \log(M_*/M_\odot) < 11.5$. The SEDs are normalized to unity at $1\ \mu$m. The color of each SED reflects the rest-frame UV flux in the normalized spectrum. Triangles indicate 1σ upper limits. The gray curve represents the best-fit SPS model to the full SED of 1255-0.

(A color version of this figure is available in the online journal.)

Table 1
Observations

ID run	Date	Exposure Time (minutes)	Seeing ($''$)
GS-2005A-Q-20	2005 May 19	85	0.9
	2005 May 27	80	1.0
	2005 May 30	80	1.0
GS-2006A-C-6	2006 Feb 24	60	0.5
GS-2007A-C-9	2007 Mar 11	360	0.5
	2007 Mar 12	330	0.4
	2007 Mar 13	340	0.5
	2007 Mar 14	390	0.6

optical spectroscopy, Cimatti et al. (2008) have derived several absorption-line redshifts, but due to the relative faintness of quiescent galaxies in the rest-frame UV these observations require ~ 100 hr of integration and result in incomplete samples. Near-infrared (NIR) spectroscopy allows the detection of the "bright" rest-frame optical continuum emission, but deep spectra are expensive due to the lack of multiplexing, the bright NIR background, and strong OH lines. Thus, so far no rest-frame optical absorption lines have been detected in NIR spectra of $z > 2$ quiescent galaxies, and previous redshift determinations rely on the detection of the Balmer and/or 4000 Å break with uncertainties of $\Delta z/(1 + z) < 0.019$ (Kriek et al. 2008b).

In this paper we present an ~ 29 hr Gemini Near-Infrared Spectrograph (GNIRS; Elias et al. 2006) spectrum of a compact, quiescent galaxy at $z = 2.1865$, allowing a detailed study of the stellar population and the detection of any rest-frame optical emission and absorption lines. Moreover, it gives us a glance into the future, as this is the deepest single-slit NIR spectrum ever taken of a $z > 2$ galaxy. Throughout the paper, we assume a ΛCDM cosmology with $\Omega_m = 0.3$, $\Omega_\Lambda = 0.7$, and $H_0 = 70$ km s^{-1} Mpc^{-1}. All broadband magnitudes are given in the Vega-based photometric system.

2. TARGET SELECTION AND DATA

The target was chosen from our GNIRS NIR spectroscopic survey for massive galaxies at $z \sim 2.3$ (Kriek et al. 2008b). All galaxies were originally selected from the Multi-Wavelength Survey by Yale-Chile (MUSYC), which provides us with deep optical-IR photometry (Gawiser et al. 2006; Quadri et al. 2007; Taylor et al. 2009b; Damen et al. 2009; Marchesini et al. 2009). These "shallow" spectra (typically ~ 3 hr of integration; see Kriek et al. 2008b) allowed us to derive continuum redshifts and classify the galaxies.

We selected 1255-0[6] from the nine massive quiescent galaxies presented in Kriek et al. (2006b), because of its redshift (the optical break falls in the J band) and its visibility at the time of our GNIRS run. The galaxy is not brighter than the other candidates. Also, its effective radius (r_e) of 0.78 kpc is very similar to the median r_e (0.9 kpc) of the other massive, quiescent galaxies in our sample (see van Dokkum et al. 2008). Figure 1 shows the image of 1255-0 as obtained by the Near-Infrared
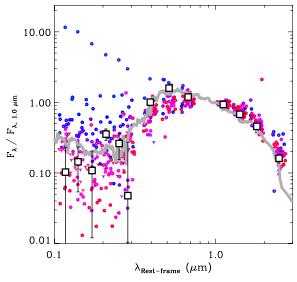
Camera and Multi-Object Spectrometer (NICMOS). Altogether, this galaxy seems typical for the general class of quiescent galaxies at $z \sim 2.3$.

We also consider how this galaxy compares to the general population of massive galaxies at similar redshift (including star-forming galaxies). In Figure 2, we compare the rest-frame UV-NIR spectral energy distributions (SEDs) of all galaxies in the deep MUSYC sample (Quadri et al. 2007; Marchesini et al. 2009) with comparable redshift and stellar mass. The redshifts are all photometric and derived using EAZY (Brammer et al. 2008). The stellar masses are derived using the code described in the Appendix, for the Maraston (2005) stellar population synthesis (SPS) models, solar metallicity, the Calzetti et al. (2000) reddening law, and a Kroupa (2001) IMF. Figure 2 illustrates that 1255-0 is slightly redder than the average massive galaxy at this redshift. This is expected given the fact that it was selected to be quiescent.

In total, we integrated nearly 29 hr on 1255-0 with GNIRS (with individual exposures of 10 minutes) divided over three observing runs in 2005 May, 2006 February, and 2007 March. The integration times and average seeing are given in Table 1. During the first three nights the conditions were mediocre, with occasional clouds and an average seeing of $1''$. The weather

---

[6] The ID number was 1256-0 and 1256-151 in Kriek et al. (2008a) and Kriek et al. (2006b), respectively.
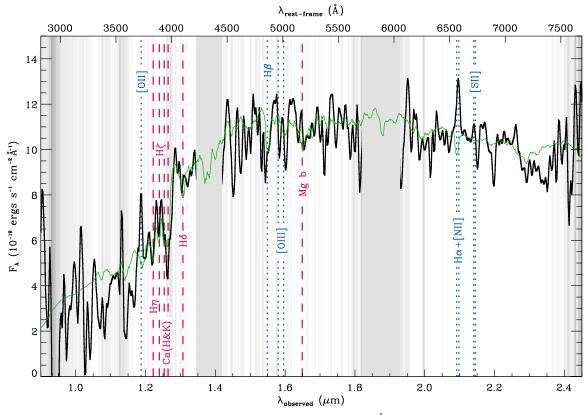
Figure 3. $\sim$ 29 hr deep GNIRS spectrum of 1255-0 (black). The spectrum is sampled to bins of 50 Å in observed frame, and smoothed by a boxcar of 75 Å. The gray shaded background indicates the noise level of the spectrum, with dark being noisier. We omitted the regions in between the atmospheric windows. Overplotted in green is the best-fit Bruzual & Charlot (2003) SPS model to the spectrum and optical-IR photometry, assuming a Chabrier (2003) IMF and solar metallicity. This fit corresponds to a stellar mass of 2.3×10^{11} $M_{\odot}$, an age of 2.1 Gyr, a τ of 0.3 Gyr, a reddening of $A_v = 0.25$ mag, an SFR of 1.9 $M_{\odot}$ yr^{-1}, and a specific SFR of 0.008 Gyr^{-1}. The locations of possible absorption and emission lines are indicated by the red dashed and blue dotted lines, respectively.

(A color version of this figure is available in the online journal.)

conditions were excellent during the last two runs, with clear skies and an average seeing of 0″.5.

The galaxy was observed in a cross-dispersed mode, in combination with the 32 lines mm^{-1} grating and the 0″.675 slit. The spectral resolution varies between $\sim$ 900 and $\sim$ 1050 over the different orders. Observations were done using an ABA′B′ on-source dither pattern, such that we can use the average of the previous and following exposures as sky frame (van Dokkum et al. 2004; Kriek et al. 2006a). Acquisition was done using blind offsets from nearby stars. Before and after every observing sequence we observe an A V0 star, for the purpose of correcting for telluric absorption. The final spectra of the two stars are combined to match the airmass of the observing sequence.

A detailed description of the reduction procedure of GNIRS cross-dispersed spectra is given in Kriek et al. (2006a). In summary, we subtract the sky, mask cosmic rays and bad pixels, straighten the spectra, combine the individual exposures, stitch the orders, and finally correct for the response function. The different observing sequences are weighted according to their signal-to-noise ratio (S/N) when being combined.

A one-dimensional spectrum is extracted by summing all adjacent lines (along the spatial direction) with a mean flux greater than 0.1 times the flux in the central row, using optimal weighting with the S/N. We extract both a high- and low-resolution spectrum with 10 Å and 50 Å per bin, respectively. The high-resolution spectrum, which is resampled such that no resolution is lost, is used for spectral features, while the low-resolution spectrum is extracted to study the continuum emission. In order to flux calibrate the spectrum, we derive

the spectroscopic J, H, and K fluxes by integrating over the corresponding filter curves. We derive one scaling factor by comparing the spectroscopic colors with the J, H, and K broadband photometric data from MUSYC. Finally, we multiply the spectrum by this scaling factor.

The low-resolution spectrum is shown in Figure 3. Note the clear detection of the rest-frame optical break in the J band and the relatively high S/N in the continuum (compared to the spectrum shown in Kriek et al. 2006b).

3. ANALYSIS

We study the properties of this galaxy in two ways, first by measuring and analyzing the spectral features (Sections 3.1 and 3.2) and second by modeling and decomposing the stellar continuum emission (Sections 3.3–3.5). Finally, in Section 3.6, we compare the deep spectrum modeling results with our previously published shallow spectrum.

3.1. Emission and Absorption Features

We measure the redshift and all emission-line properties by modeling the extracted high-resolution (10 Å per bin) one-dimensional spectrum. We detect Hα, [N II] $\lambda\lambda6583$, and [S II] $\lambda\lambda6717$ in the K band. The bottom panels of Figures 4 and 5 show the relevant part of the two-dimensional and one-dimensional spectra, respectively. For the former, we first removed the best-fit continuum model (see Section 3.3) to make the lines more visible. We detected none of these lines in our shallow spectrum (Kriek et al. 2006b), as they are too faint.
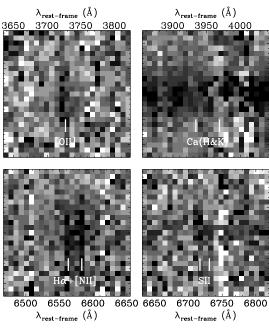
Figure 4. Selected regions of the two-dimensional spectrum. Each pixel is 25 Å in observed frame (8 Å in rest-frame) in the wavelength (horizontal) direction by 0″.15 in the spatial (vertical) direction. The top-left, bottom-left, and bottom-right panels show the emission lines [O II], Hα and [N II], and [S II], respectively. The continuum emission has been removed, using the best-fit model, to make the lines more visible. The top-right panel shows the wavelength region around the break. Ca II-H and Ca II-K are clearly visible in the two-dimensional spectrum. In this panel, the continuum emission has not been removed.

Figure 5. One-dimensional spectrum (10 Å per bin in observed frame) in regions around the emission lines. F_λ is in 10^{-19} erg s^{-1} cm^{-2} Å^{-1}. The red and blue lines represent the best continuum and emission-line fits, respectively. While we detect [O II], Hα, [N II] and [S II], we see no signs of Hβ in emission or the two [O III] lines.

(A color version of this figure is available in the online journal.)

We model Hα and the two [N II] lines simultaneously, by assuming the same redshift and width for all three lines, the best-fit continuum model as derived in Section 3.3, and Gaussian profiles. As the detected emission lines are all faint, it is important to accurately correct for continuum emission (including the Balmer absorption lines). The continuum model is corrected for the spectral resolution of GNIRS and convolved to the same velocity width as the emission-line model. Furthermore, we adopt the ratios of transition probability between the two [N II] lines of 0.34.

We derive the best values for the redshift, line width, and the fluxes of the emission lines by minimizing χ^2. The uncertainties on the modeling results are derived using 500 Monte Carlo
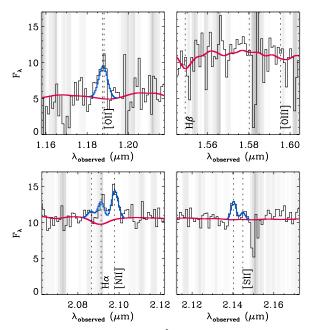
simulations. In the simulations, we perturb the measured spectrum using the noise spectrum. The results are listed in Table 2. [S II] λλ6717 and [S II] λλ6731 are modeled in the same way; thus the redshift, width, and scaling for both lines were free parameters.

In the H band, we detect no emission lines (see Figure 5 (top-right panel)). We derive 2σ upper limits using 500 Monte Carlo simulations in which we model the lines assuming the width and redshift as obtained from the Hα and [N II] lines, and the continuum model. We fit all three expected lines Hβ, [O III] λλ4959, and [O III] λλ4959 simultaneously, assuming a ratio of 0.33 between the two [O III] lines. Upper limits are derived from the best-fit results of all simulations.

In the J band, we detect the doublet [O II] (see Figures 4 and 5 (top-left panels)). We do not resolve the two lines separately,

Table 2
Spectral Features

Lines	λ (Å)	EWs (Å)	F (10^{-17} erg s^{-1} cm^{-2})	L (10^{42} erg s^{-1})	z	σ[d] (km s^{-1})
[O II][a]	3727	$14.8^{+1.8}_{-2.0}$	$2.24^{+0.31}_{-0.36}$	$0.87^{+0.11}_{-0.13}$	...	522^{+88}_{-185}
Hβ[a,b,c]	4863	< 1.3	< 0.42	< 0.15	...	...
[O III][a,b]	4959	< 0.4	< 0.14	< 0.05	...	...
[O III][a,b]	5007	< 1.3	< 0.43	< 0.15	...	...
[N II]	6548	$1.7^{+0.1}_{-0.1}$	$0.55^{+0.05}_{-0.03}$	$0.20^{+0.02}_{-0.01}$	$2.1865^{+0.0002}_{-0.0002}$	203^{+26}_{-15}
Hα[c]	6563	$4.0^{+0.5}_{-0.6}$	$1.29^{+0.16}_{-0.18}$	$0.46^{+0.06}_{-0.06}$	$2.1865^{+0.0002}_{-0.0002}$	203^{+26}_{-15}
[N II]	6583	$5.1^{+0.4}_{-0.3}$	$1.66^{+0.14}_{-0.09}$	$0.60^{+0.05}_{-0.03}$	$2.1865^{+0.0002}_{-0.0002}$	203^{+26}_{-15}
[S II]	6717	$2.3^{+0.2}_{-0.3}$	$0.76^{+0.08}_{-0.08}$	$0.27^{+0.03}_{-0.03}$	$2.1864^{+0.0003}_{-0.0002}$	108^{+25}_{-34}
[S II]	6731	$0.9^{+0.3}_{-0.2}$	$0.28^{+0.10}_{-0.07}$	$0.10^{+0.04}_{-0.03}$	$2.1864^{+0.0003}_{-0.0002}$	108^{+25}_{-34}

Notes.
[a] Fixed to best z_{spec} as derived from Hα and [N II].
[b] Fixed to best σ as derived from Hα and [N II].
[c] Corrected for Balmer absorption.
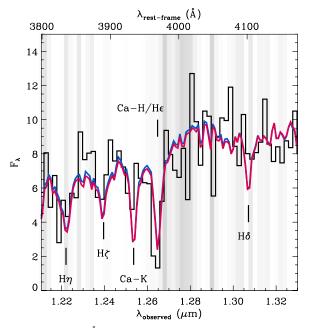[d] The resolution of GNIRS is $R \sim 1000$, corresponding to $\sigma = 128$ km s^{-1}.

Figure 6. Spectrum (20 Å per bin in observed frame) in the wavelength region around the rest-frame optical break. F_λ is in 10^{-19} erg s^{-1} cm^{-2} Å^{-1}. The red and blue curves represent the best fits for supersolar (2.5 $Z_\odot$) and solar metallicity, respectively. Both the Ca II-H/Hϵ and Ca II-K lines are detected, as well as Hη and Hζ.

(A color version of this figure is available in the online journal.)

and thus we fix the ratio (to 1) and redshift when fitting the lines. The combined fitting parameters are given in Table 2.

For each pair of lines we fit simultaneously, we assume that all line emission originates from the same physical region. [S II] and Hα yielded consistent redshifts, but the different combinations of lines resulted in different widths. This might imply that the lines originate from different processes and regions in the galaxy. However, the lines are all faint, and the errors on the line widths are probably somewhat underestimated because of our fitting procedure (allowing more freedom in the fits would result in larger uncertainties, particularly in the linewidths). Furthermore, we do not know the relative contributions from the two [O II] line. Thus, we cannot draw any firm conclusion from the different line widths.

As far as we are aware of, this is the first rest-frame optical spectrum of a quiescent galaxy beyond $z = 2$ for which rest-frame optical absorption lines are detected. Figure 6 shows that we detect Hη, Hζ, Ca II-K, and Ca II-H/Hϵ. Ca II-K and Ca II-H/Hϵ are also visible in the top-right panel of Figure 4. In Figure 6, we also show the best-fit Bruzual & Charlot (2003) models for fixed solar metallicity and when leaving the metallicity as a free parameter (see Section 3.3). Furthermore, the absorption lines Mg b $\lambda5175$ and Hβ are detected in the low-resolution spectrum in Figure 3. There might also be a hint for Hδ in Figure 3. However, a significant detection of this line requires an even deeper spectrum.

This deep spectrum allows an accurate measure of the strength of the 4000 Å break, which is an indicator of the evolution stage or age of the stellar population. We use the definition of Balogh et al. (1999) to measure the strength of this break, and find a value of $D_n(4000) = 1.40^{+0.03}_{-0.03}$. The corresponding age depends on the star formation history (SFH), the metallicity, and the dust content of the galaxy. For the extreme case of a simple stellar population (SSP) model with solar metallicity, an age of ~ 0.6 Gyr is needed to produce such a break. Assuming little or no

dust, this value can be seen as a lower limit on the population age. A more detailed measurement of the age of the stellar population will be given in Section 3.3.

3.2. Ionization Mechanism

Emission-line ratios can be used to study the origin of the ionized emission. In particular, [N II]/Hα, which reflects both the metallicity and ionization parameter U of a galaxy, is a powerful discriminator. Ratios of [N II]/H$\alpha > 1$ suggest that an object is ionized by a hard radiation field; H II regions are not able to produce such high ratios (Kewley et al. 2001). The ratio of [S II]/Hα[7] can be used for a similar purpose, as H II regions have [S II]/H$\alpha < 0.6$. The high values for both [N II]/Hα and [S II]/Hα of $1.3^{+0.3}_{-0.2}$ and $0.8^{+0.2}_{-0.2}$ respectively show that normal star-forming regions are not the dominant contributor to the line emission in this galaxy.

The ratio of [O III]/[O II] can be used to further characterize the hardness of the ionizing radiation field (Shields 1990; Kewley & Dopita 2002). [O III] $\lambda\lambda5007$ is not detected in our spectrum, but we derive a 2σ upper limit on this parameter. We find $\log(\text{[O III]/[O II]}) < -0.89$, implying an ionization parameter $U < 10^7$ (Kewley et al. 2001). This ratio is consistent with the original definition for low-ionization nuclear emission-line regions (LINERs) of [O II]/[O III] > 1, and so the line emission in 1255-0 is most likely caused by a LINER.

The origin of LINER emission has been a subject of debate since its original classification as an active galactic nucleus (AGN) class by Heckman (1980). Although there is substantial evidence that many LINERs are powered by accretion onto massive black holes, LINER emission can also originate from a young starburst or by shock heating through cloud collisions induced by galaxy mergers or starburst-driven winds (e.g., Dopita & Sutherland 1995). Because the SFR in 1255-0 is very low (see Section 3.3), a starburst or starburst-driven wind is unlikely to cause the LINER emission, and thus a low-luminosity AGN is the more likely option. Nonetheless, even if the observed LINER emission does not originate from black hole accretion, it is still the case that normal star-forming regions do not dominate the observed line emission.

Finally, we note that the line widths are not necessarily indicative of the depth of the gravitational potential, as in the local universe there is a large scatter between the gas line widths of LINERs and the velocity dispersion of the stars of their host galaxies (Greene & Ho 2005).

3.3. Modeling the Continuum Emission

We study the nature of the stellar population by comparing the spectrum with the SPS models of Bruzual & Charlot (2003) and Maraston (2005), using the code described in the Appendix. We assume an exponentially declining SFH with timescale τ, a Chabrier (2003) or Kroupa (2001) IMF, and the Calzetti et al. (2000) reddening law. We derive model spectra for a grid with τ between 10 Myr and 10 Gyr in steps of 0.1 dex, A_V between 0 and 3 mag in steps of 0.05 mag, and age in steps of 0.02 dex with a minimum age of 10 Myr and the maximum age not exceeding the age of the universe. The metallicity when fitting the Maraston (2005) model is fixed to solar ($Z = 0.02$), but for the Bruzual & Charlot (2003) models we vary the metallicity, among subsolar ($Z = 0.004$), solar, and supersolar ($Z = 0.05$). The redshift is fixed to $z = 2.1865$ as derived from the emission lines

---

[7] For [S II] we take the sum of both lines, while for the ratio of [N II]/Hα only [N II] $\lambda\lambda6583$ is used.

Table 3
Stellar Population Properties

UBVRIz + NIR Spectrum	Log M_* ($M_\odot$)	Log Age (yr)	Log τ (yr)	A_V (mag)	Z	Log SFR ($M_\odot$ yr^{-1})	Log SFR/M_* (Gyr^{-1})
BC03, Chabrier, $Z_\odot$	$11.36^{+0.00}_{-0.04}$	$9.34^{+0.02}_{-0.04}$	$8.5^{+0.0}_{-0.1}$	$0.20^{+0.15}_{-0.05}$	$0.02^{+0.00}_{-0.00}$	$0.19^{+0.16}_{-0.20}$	$-2.17^{+0.17}_{-0.18}$
BC03, Chabrier, Z free	$11.26^{+0.00}_{-0.02}$	$9.10^{+0.02}_{-0.02}$	$8.3^{+0.0}_{-0.1}$	$0.30^{+0.05}_{-0.05}$	$0.05^{+0.00}_{-0.00}$	$0.45^{+0.00}_{-0.36}$	$-1.81^{+0.00}_{-0.34}$
BC03, Chabrier, $Z_\odot$, +IRAC	$11.36^{+0.00}_{-0.04}$	$9.32^{+0.04}_{-0.04}$	$8.5^{+0.0}_{-0.1}$	$0.25^{+0.10}_{-0.10}$	$0.02^{+0.00}_{-0.00}$	$0.28^{+0.07}_{-0.29}$	$-2.08^{+0.08}_{-0.27}$
BC03, Chabrier, Z free +IRAC	$11.26^{+0.00}_{-0.02}$	$9.10^{+0.02}_{-0.02}$	$8.3^{+0.0}_{-0.1}$	$0.30^{+0.00}_{-0.10}$	$0.05^{+0.00}_{-0.00}$	$0.45^{+0.00}_{-0.36}$	$-1.81^{+0.00}_{-0.34}$
MA05, Kroupa, $Z_\odot$	$11.24^{+0.00}_{-0.02}$	$9.26^{+0.00}_{-0.02}$	$8.4^{+0.0}_{-0.1}$	$0.00^{+0.05}_{-0.00}$	$0.02^{+0.00}_{-0.00}$	$0.01^{+0.11}_{-0.42}$	$-2.23^{+0.12}_{-0.40}$
MA05, Kroupa, $Z_\odot$ +IRAC	$11.24^{+0.00}_{-0.04}$	$9.26^{+0.00}_{-0.04}$	$8.4^{+0.0}_{-0.1}$	$0.00^{+0.10}_{-0.00}$	$0.02^{+0.00}_{-0.00}$	$0.01^{+0.20}_{-0.42}$	$-2.23^{+0.21}_{-0.40}$

Notes. When deriving the confidence intervals, we only use the model grid points enclosed by the 68% χ^2 threshold values (see the Appendix). Due to this discretization, nonzero confidence intervals may be rounded to zero.

(see Section 3.1). We fit the low-resolution one-dimensional spectrum (50 Å per bin in observed frame) and search for the best solution by minimizing χ^2.

In contrast to our previous studies (Kriek et al. 2006a, 2006b, 2008b), we do not mask regions with low atmospheric transmission or strong sky emission when fitting the spectrum. As the S/N of this spectrum is considerably higher than in Kriek et al. (2008b), we apply a much smaller bin size. Bins in bad wavelength regions will have larger uncertainties and thus simply have lower weight in the fit. When using larger bins (400 Å in Kriek et al. 2008b) this method is less appropriate, as a bad region will contaminate nearly all bins.

To further constrain the SFR, we include the rest-frame UV broadband photometry. Furthermore, we extend the SED into the rest-frame NIR using IRAC photometry (Marchesini et al. 2009). The rest-frame NIR helps to constrain the stellar mass and age of the galaxy (e.g., Labbé et al. 2005; Shapley et al. 2005; Wuyts et al. 2007; Muzzin et al. 2009). However, as the SPS models are still uncertain in this regime, we fit the galaxy both with and without the IRAC photometry.

We derive 68% confidence intervals on all stellar population properties using 200 Monte Carlo simulations, as described in the Appendix. The photometric uncertainties are increased using the template error function, which accounts for uncertainties in the model templates as a function of the rest-frame wavelength (Brammer et al. 2008). Furthermore, we apply the automatic scale option, such that for each simulation the simulated spectrum is calibrated using the simulated J, H, and K photometry (see Section 2 and the Appendix). Thus, the uncertainty in the calibration of the spectrum is explicitly taken into account.

In Table 3 we give all modeling results for the different SPS libraries, free or fixed metallicity, and with or without IRAC. In Figure 3, we show the spectrum and best-fit Bruzual & Charlot (2003) model with solar metallicity. The continuum fitting implies a stellar mass of $\sim 2 \times 10^{11}\ M_\odot$, a reddening of $A_V = 0.0$–0.3 mag, a star formation timescale of $\tau \sim 0.3$ Gyr, an age (since the onset of star formation) of 1.3–2.2 Gyr, and an SFR of 1–3 $M_\odot$ yr^{-1}. The universe is 3 Gyr at $z \sim 2.1865$, which implies a formation redshift $z_{\rm form} = 4$–7.

It is remarkable how well constrained the formal confidence intervals are. However, the formal errors do not reflect the true uncertainties properly, as they are dominated by the systematic effects such as the assumptions concerning the SPS models, the SFH, metallicity, and extinction law (see, e.g., Shapley et al. 2001; Wuyts et al. 2007; Kannappan & Gawiser 2007; Conroy et al. 2009; Muzzin et al. 2009, for more discussion on this topic). For the Bruzual & Charlot (2003) models, supersolar metallicity is formally preferred above solar. We do not believe the fact that
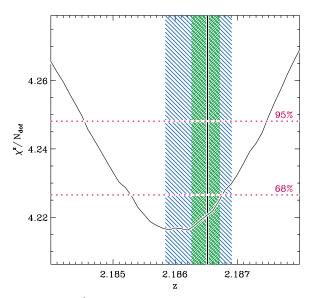

Figure 7. Reduced χ^2 vs. continuum redshift (number of degrees of freedom $N_{\rm dof} = 319$), when leaving redshift as a free parameter in the SPS model (Bruzual & Charlot 2003) fitting. The other parameters, including metallicity, are allowed to vary. The rest-frame UV-NIR broadband photometry is not included in the fit. The 68% and 95% confidence intervals are indicated by the dotted lines. The best-fit emission line redshift is indicated by the vertical solid line, and its 68% and 95% confidence intervals by the green and blue shaded regions, respectively. The continuum emission yields a well constrained spectroscopic redshift. The redshift difference between the stellar and nebular emission is not at all significant.

(A color version of this figure is available in the online journal.)

this result is significant, due to the strong degeneracy between age and metallicity, and the uncertainties in the SPS model, and so the metallicity could well be less, e.g., solar. Nonetheless, the different models are surprisingly consistent. The inclusion or exclusion of IRAC has little effect on the modeling results for this deep spectrum (see Muzzin et al. (2009) for a general discussion of the inclusion of IRAC data in the modeling of $z \sim 2.3$ galaxies with shallower spectroscopy).

The detection of the strong break and absorption features allows the measurement of a stellar continuum redshift. We use the same fitting procedure as described above; only this time, we leave the redshift as a free parameter. Furthermore, we fit only the spectrum; thus, the rest-frame UV and NIR broadband photometric data are not included. In Figure 7, we show the reduced χ^2 as a function of redshift. We find a stellar redshift of $z = 2.1862^{+0.0005}_{-0.0009}$. The emission-line redshift is also indicated in this figure. There is no evidence for a significant redshift offset between the stellar and nebular emission. Nonetheless,

we cannot exclude a possible offset, due to the relatively large uncertainties on the continuum redshift.

3.4. A Recent Starburst?

When modeling the SED by SPS models, we assume an exponentially declining SFH. However, this is a simplification, and more complex SFHs are more realistic. For example, subsequent merging is expected to result in central dissipational starbursts (e.g., Hopkins et al. 2009b). This would result in a younger stellar population in the central part of the galaxy, with a lower mass-to-light ratio (M/L) than the older underlying population. Similarly, if the galaxy experienced recent star formation in a disk-like component, the galaxy is composed of an old central concentration and a more extended young component. This younger population will contribute relatively more to the observed light than to the stellar mass.

In order to assess whether a recent starburst took place and how much it may contribute to the stellar mass of the galaxy, we investigate how much of the light can be accounted for by a 0.5 Gyr SSP model, with 0.25 mag of visual extinction (see Table 3). We choose a post-starburst instead of an ongoing starburst, as we know that the current global SFR in the galaxy is very low. We subtract different mass contributions and apply the same fitting procedure as discussed in Section 3.3. The maximum contribution of the post-starburst population is set by the rest-frame UV flux, and shown by the red SED in the top panel of Figure 8. Up to $\sim 10\%$ of the stellar mass may have been formed in a recent starburst. Due to the relatively low M/L of this post-starburst population, the contribution to the H-band light is much larger ($\sim 40\%$).

In the inset of the top panel of Figure 8, we show the reduced χ^2 of the best-fit SPS model to the corrected spectrum and photometry, for different mass fractions of the post-starburst stellar population. Models with a mass fraction between ~ 0 and 5% provide equally good fits, while higher mass fractions result in worse agreement. The red line indicates the maximum contribution, corresponding to the red SED. Thus, while this galaxy may have experienced a recent starburst, both the light and the stellar mass are dominated by an older stellar population. Nonetheless, it still remains to be explored how much the light distribution may be different from the stellar mass distribution in these compact quiescent galaxies.

3.5. Continuum Emission from an AGN?

In Section 3.2, we found that the line emission of 1255-0 is of LINER origin. This raises the question of whether an AGN may contribute to the continuum emission of 1255-0. We investigate this by subtracting different AGN contributions and fitting the corrected SED by SPS models. We assume a power-law SED for the AGN. The maximum AGN contribution is set by the rest-frame UV fluxes in combination with the 8 μm IRAC band, and shown by the green line in the bottom panel of Figure 8. The corresponding contribution to the H-band flux is $\sim 8\%$.

In the inset of the bottom panel of Figure 8, we show the reduced χ^2 of the best-fit SPS model for different assumed AGN contributions. The green line indicates the maximum contribution, corresponding to the green SED. The fit clearly worsens for an increasing AGN contribution. Altogether, an AGN is unlikely to contribute significantly to the continuum emission and is limited to a maximum of $\sim 8\%$ to the H band.
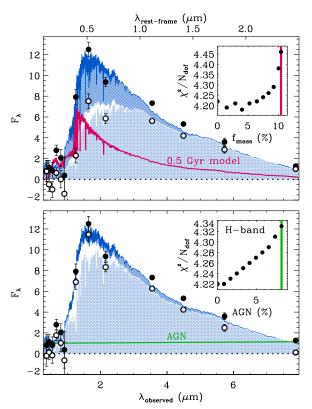

Figure 8. Multicomponent modeling of 1255-0. The black solid dots and blue SEDs show the original broadband photometric data and best-fit SPS model to the full SED (including NIR spectrum). In the top panel we assess the contribution from a post-starburst population (with an A_V of 0.25 mag), which can account for $< 10\%$ of the stellar mass and $< 40\%$ of the H-band flux. The corrected SED and corresponding best-fit SPS model are represented by the open symbols and white curve, respectively. The inset shows the quality of the fit as a function of the contribution of the post-starburst population to the total stellar mass. The red lines indicate the maximum contribution. In the bottom panel, we assess a contribution from an AGN. The inset shows the quality of the fit as a function of the AGN contribution to the H-band flux. The green lines indicate the maximum contribution (8%). In both cases, these fits imply that the galaxy is primarily composed of an evolved stellar population.

(A color version of this figure is available in the online journal.)

3.6. Comparison to the Shallow Spectrum

While our 5 hr[8] shallow spectrum of 1255-0 presented in Kriek et al. (2008a) provided a similar stellar mass and SFR (when corrected for the difference in the assumed IMF), the age, the dust content, and the continuum redshift differ by $\sim 2\sigma$ compared to the 29 hr deep spectrum. Our shallow spectrum of 1255-0 yields a continuum redshift of $2.31^{+0.05}_{-0.07}$, an age of $0.57^{+0.44}_{-0.28}$ Gyr, and an A_V of $1.2^{+0.6}_{-0.6}$ mag. Thus, this galaxy was previously classified as a dusty post-starburst galaxy, at slightly higher redshift. In the fit to the shallow spectrum the dominant optical break was thought to be the Balmer jump, while in our deeper spectrum the 4000 Å break is found to be the more prominent one. If we fit the shallow spectrum of 1255-0 with the redshift fixed to $z = 2.1865$, we find a significantly older age of 2.9 Gyr and a lower A_V of 0.35 mag.

The change in redshift also influences the rest-frame color determination (see Kriek et al. 2008a). 1255-0 was among our reddest galaxies, with a rest-frame $U-B$ color of $0.36^{+0.05}_{-0.06}$ mag. The deep spectrum yields an $U-B$ color of 0.52 mag. However,

---

8   The weather conditions during the first runs were significantly worse, and the effective exposure time is closer to 1–2 hr.

if we use the same method as in Kriek et al. (2008a), thus determining the color of the best fit, we find $U - B = 0.30$. This difference is likely caused by the discrepancy between the spectrum and the fit around 1.15 μm.

We do not expect the full sample of shallow spectra to suffer as severely from this degeneracy between redshift and stellar population as 1255-0. In Kriek et al. (2008b) we apply the same continuum fitting procedure to the emission-line galaxies in our sample, and find a good agreement between the emission-line and continuum redshifts. This sample contained several galaxies with SED shapes similar to those without emission lines. Nonetheless, while it seems more likely that 1255-0 is the largest outlier ($\sim 2\sigma$), caution is required. This case illustrates that more deeper spectra are needed.

4. THE STAR FORMATION ACTIVITY IN 1255-0

Comparison of the stellar continuum emission with SPS models (Section 3.3) confirms our earlier results that the SFR in 1255-0 is strongly suppressed (Kriek et al. 2006b). Depending on the SPS library and the assumed metallicity, the best-fit SFR is 1–3 $M_\odot$ yr^{-1}. As expected for a galaxy with low-level star formation, the total dust extinction is low with values of A_V of 0.0–0.3 mag.

The low SFR is independently confirmed by the emission-line diagnostics. In the previous section, we noted that star-forming regions cannot be the dominant contributor to the line emission. Nevertheless, if we assume that the detected Hα emission is caused by just star formation, we can use the calibration

$$\text{SFR} \ (M_\odot \ \text{yr}^{-1}) = 7.9 \times 10^{-42} \ L_{\text{H}\alpha} \ (\text{erg s}^{-1}) \qquad (1)$$

as given by Kennicutt (1998) to derive the SFR from the Hα luminosity. Assuming no dust extinction, the observed luminosity would result in an SFR of $4.0^{+0.4}_{-0.6}$ $M_\odot$ yr^{-1} for a Salpeter (1955) IMF. This value would decrease by a factor of ~ 1.8 for a Chabrier (2003) or Kroupa (2001) IMF, but increases by a factor of ~ 2.3 if there is 1 mag of visual extinction in the star forming regions. Although we have a good constraint on the total attenuation of the galaxy from the spectral modeling ($A_V = 0.0$–0.3 mag), it is difficult to estimate the extinction in the line-emitting regions without measuring a Balmer decrement. The combination of Hα and the 2σ upper limit on Hβ gives a 2σ lower limit on the ratio of Hα/Hβ of 3.07. This limit is close to the intrinsic ratio for H II regions of 2.76, and thus sets no constraints on the dust content. Nonetheless, even when assuming that the line emission originates just from star formation, and assuming 1 mag of dust extinction in the H II regions, the obtained SFR is still only ~ 4 $M_\odot$ yr^{-1} (for a Chabrier IMF).

The best-fit stellar mass of 1255-0 is $(1.7$–2.3$) \times 10^{11}$ $M_\odot$. This value is slightly dependent on the choice for the SPS model and on whether metallicity is assumed to be solar or left as a free parameter. If left as a free parameter, supersolar is preferred over solar, although we argue in Section 3.3 that this result is not significant. The best-fit star formation timescale is 0.2–0.3 Gyr, and the best-fit stellar age is 1.8–2.2 Gyr and ~ 1.3 Gyr for solar metallicity and supersolar metallicity, respectively. The age of the universe at this redshift is 3.0 Gyr and the formation redshift is $z_{\text{form}} \sim 4$–7.

We study the evolution stage of the galaxy by means of the quenching factor q_{sf}, which measures by what factor the SFR has been reduced compared to the past average SFR. We define

q_{sf} as follows:

$$q_{\text{sf}} = 1 - \frac{\text{SFR}_{\text{current}}}{\text{SFR}_{\text{past}}} = 1 - \frac{\text{SFR}_{\text{current}}}{\frac{M_*}{\text{age}}}. \qquad (2)$$

In this equation M_* is not the current stellar mass, but all the mass formed in the galaxy. This quenching factor is related to the ratio of the age to the star formation timescale τ (i.e., how many e-folding times have been passed since the galaxy was formed) in the following way:

$$q_{\text{sf}} = 1 - \frac{\text{age}}{\tau} \frac{e^{-\frac{\text{age}}{\tau}}}{1 - e^{-\frac{\text{age}}{\tau}}}. \qquad (3)$$

Because age/τ is a relatively well constrained parameter, q_{sf} is a fairly robust measure for the evolution stage of a galaxy. We note that Davé (2008) defined a comparable factor: the star formation activity parameter $\alpha_{\text{sf}} = (M_*/\text{SFR})/(t_H - 1\text{Gyr})$. Instead of using the best-fit age of the galaxy, this parameter uses the Hubble time (t_H) minus 1 Gyr.

1255-0 has a q_{sf} of $0.991^{+0.007}_{-0.002}$. Thus, the SFR in this galaxy has been reduced by more than 99% and the current SFR is less than 1% of the average past SFR. This implies that the star formation has been strongly quenched since the major star formation epoch. Furthermore, in Section 3.4, we found that a 500 Myr SSP accounts for $< 10\%$ of the stellar mass, which implies that at least 90% of the stellar mass is in stars older than 0.5 Gyr, and thus formed beyond $z = 2.6$.

5. DISCUSSION AND CONCLUSIONS

Due to the introduction of large photometric surveys with deep NIR imaging (e.g., Labbé et al. 2003; Franx et al. 2003), many quiescent massive galaxies beyond $z = 2$ have been identified in the past few years (e.g., Förster Schreiber et al. 2004; Daddi et al. 2004a, 2004b; Labbé et al. 2005). Moreover, these galaxies are typically found to be ultra-compact, with stellar densities that are about 2 orders of magnitude larger than in local early type galaxies of similar mass (e.g., Trujillo et al. 2006, 2007; Zirm et al. 2007; Toft et al. 2007; Longhetti et al. 2007; van Dokkum et al. 2008; Cimatti et al. 2008)

Follow-up spectroscopic studies have tried to verify the broadband photometric redshifts and stellar population properties of these ultra-dense quiescent galaxies. This turned out to be extremely difficult, and with optical spectroscopy tens to hundreds of hours are required (Daddi et al. 2005; Cimatti et al. 2008), due to their relative faintness in the rest-frame UV. Evolved galaxies beyond $z = 2$ are much brighter at NIR wavelengths, corresponding to the rest-frame optical. In Kriek et al. (2006b), we used the Balmer and/or 4000 Å breaks to obtain redshift estimates for a sample of nine massive quiescent galaxies. However, exact redshift measurement from rest-frame optical absorption lines remained out of reach until this paper.

By integrating for nearly 30 hr with GNIRS, we succeeded in detecting for the first time rest-frame optical absorption lines in an NIR spectrum of a compact, quiescent galaxy beyond $z = 2$. This deep spectrum has full NIR coverage (~ 1.0–2.4 μm). In addition to the absorption features Hη, Hζ, Ca II-K, Ca II-H/Hϵ, Hβ, and Mg b, we have detected [O II], Hα, [N II], and [S II] in emission. All emission lines are faint with luminosities of $(0.1$–0.9$) \times 10^{42}$ erg s^{-1}. The redshifts derived from the stellar continuum and from the emission lines are consistent within the uncertainties.

Comparison of the spectral continuum emission and the rest-frame UV-NIR photometry with SPS models implies a stellar mass of $\sim 2 \times 10^{11}$ $M_\odot$, a reddening of $A_V = 0.0$–0.3 mag, a star formation timescale of $\tau = 0.2$–0.3 Gyr, and an age of 1.3–2.2 Gyr. The results are slightly different for the different SPS models and different assumed metallicities. We find a low SFR of about 1–3 $M_\odot$ yr^{-1}, implying that the star formation is strongly quenched and reduced by more than 99% since its major star formation epoch. If this galaxy is typical for quiescent galaxies, quenching of star formation is extremely efficient. The constraints on the SFR are very tight, and compared to the previously published shallow spectrum of this galaxy (Kriek et al. 2008b) they are more stringent by a factor of ~ 8.

We do detect a faint Hα emission line, which, based on emission-line diagnostics, is not caused by stellar ionization. However, even if we assume that the Hα line was due to star formation, it would result in a low SFR of ~ 2–4 $M_\odot$ yr^{-1}. One possibility is that obscured star formation may have been missed. However, at low redshift there is a strong correlation between the dust-corrected luminosity of Hα and the bolometric luminosity (e.g., Moustakas et al. 2006). Reddy et al. (2006) found a similar relation at high redshift. Thus, based on the faint Hα line, the nature of the line emission, and the lack of a detection at 24 μm (I. Cury 2009, private communication), we do not expect this galaxy to host obscured ongoing starburst regions.

Although we can confirm our earlier conclusions about the quiescent nature of the stellar population in 1255-0 (Kriek et al. 2006b), we previously underestimated the age. The shallower spectrum showed an apparent Balmer break and our fit preferred a younger dusty post-starburst galaxy. However, our deeper spectrum shows that the galaxy is 1.3–2.2 Gyr old, and the optical break is dominated by the 4000 Å break rather than the Balmer jump. A post-starburst (0.5 Gyr) population can only account for $\lesssim 10\%$ of the stellar mass.

The underestimated age in the shallow spectrum is related to the overestimation of the continuum redshift. In Kriek et al. (2008b) we found a continuum redshift of $2.31^{+0.05}_{-0.07}$, which is within 2σ consistent with the emission-line redshift of 1255-0. This may imply that the uncertainties in our previous work are underestimated. However, comparison of emission-line and continuum redshifts for 19 emission-line galaxies in Kriek et al. (2008b) demonstrated the reliability of the uncertainties of our continuum redshifts, and thus 1255-0 is probably "the" largest (2σ) outlier.

The fact that we previously underestimated the age of the galaxy shows how difficult it is to estimate ages based on "shallow" spectra, let alone broadband photometry. Thus, we cannot exclude that the ages of more quiescent galaxies may have been systematically underestimated in Kriek et al. (2008b). The best-fit models imply a formation redshift of $z = 4$–7 for 1255-0, and this may indicate that massive galaxies with strongly suppressed star formation exist at even earlier times.

The rest-frame optical emission-line diagnostics indicate that 1255-0 most likely hosts a LINER. In Kriek et al. (2007), we found that at least 4 out of the 11 emission-line galaxies in our massive galaxy sample at $2.0 < z < 2.7$ host an AGN. This study was based on relatively shallow spectroscopy (~ 3 hr per galaxy). For 1255-0, we did not detect any emission lines in the shallow NIR spectrum (Kriek et al. 2006b). Thus, we may find actively accreting black holes in more massive galaxies, when we obtain deeper data. This suggests the possibility that low luminosity AGNs may be very common in these objects.

Although an AGN dominates the line emission, its contribution to the continuum emission is very low. In the H band, in which we measured the compact size of 1255-0 (van Dokkum et al. 2008) the contribution is $\lesssim 8\%$. Thus, an AGN could not be the dominant cause for the compact size of this galaxy. A central post-starburst population may have a larger effect on our size measurements. If the stellar population in the center has a lower M/L than the outskirts, the size will appear smaller. Similarly, if the galaxy experienced recent star formation in the outer parts, the M/L will be higher in the center, and thus the size will appear larger. Although a post-starburst population can only account for $\lesssim 10\%$ of the stellar mass, it can make up $\sim 40\%$ of the H-band flux. Thus, depending on where this post-starburst population is situated, the light distribution in these compact galaxies may be more or less concentrated than the stellar mass distribution, and our size measurements may be over- or underestimated. However, regardless of whether or not a post-starburst or AGN is present, this spectrum shows that this compact quiescent galaxy is not actively forming new stars, and is primarily composed of an evolved stellar population.

The future generation of NIR spectrographs promises higher throughput, in combination with multiplexing. This will allow even deeper spectra of larger samples. However, the most spectacular results—in particular with regard to kinematic measurements of quiescent galaxies—are expected to come from NIRSPEC on the *James Webb Space Telescope* (*JWST*). Without the hindrance of the Earth's atmosphere, it will be possible to obtain significantly deeper spectra in only a small fraction of the exposure time needed for the spectrum presented in this paper.

APPENDIX

FITTING AND ASSESSMENT OF SYNTHETIC TEMPLATES

We developed a custom IDL code named FAST, to fit SPS models to broadband photometry, spectra, or both. FAST is compatible with the photometric redshift code EAZY (Brammer et al. 2008), such that the format of the input photometric catalog and filter files is similar. Optionally, the photometric redshifts as derived by EAZY can be read in and used by FAST.

Summarized, FAST reads in a parameter file, which defines the photometric and spectroscopic catalogs, the SPS models (choice from Bruzual & Charlot 2003; Maraston 2005), the IMF

(choice from Salpeter [1955](#); Kroupa [2001](#); Chabrier [2003](#)), the reddening law, and the fitted grid of stellar population properties. For all properties (age, star formation timescale τ, dust content A_V, metallicity, and redshift) the minimum and maximum value, and the step size can be defined. Optionally, FAST can calibrate spectra using the broadband fluxes.

FAST generates a six-dimensional cube of model fluxes for the full stellar population grid and all filters, spectral elements, or both. To determine the best-fit parameters, it simply determines the χ^2 of every point of the model cube. In case spectroscopic or photometric redshifts are provided, the redshift will be fixed to the closest value in the grid.

The confidence levels are calibrated using Monte Carlo simulations. The number of simulations can be defined in the parameter file. The observed fluxes are modified according to their photometric and spectroscopic errors in each simulation. Optionally, a rest-frame template error function (see EAZY; Brammer et al. [2008](#)) can be added to the broadband photometric fluxes, to account for uncertainties in the models. In case the automatic scale option is used, the spectrum is scaled individually for each simulation. By doing this, we incorporate the error on the scaling factor.[9] We determine the best solution for all simulations and define the $\chi^2_{1\sigma}$ ($\chi^2_{2\sigma}$ or $\chi^2_{3\sigma}$) level as the χ^2 value in the originally grid that encloses 68% (95% or 99%) of the simulations. The uncertainties on the stellar population properties are the minimum and maximum values that are allowed within the $\chi^2_{1\sigma}$ ($\chi^2_{2\sigma}$ or $\chi^2_{3\sigma}$) threshold.

In case photometric redshifts (as provided by EAZY) are assumed, the calculation of the confidence intervals is slightly more complicated. Both codes use different template sets and thus produce different probability distribution functions of z. Unfortunately, there is no perfect method to determine the confidence levels for this case. We use the following method, which incorporates the confidence levels of EAZY, and is fast and user friendly. We run all Monte Carlo simulations at the best-fit $z_{\rm phot}$ as derived by EAZY. We determine $\Delta\chi^2$; the difference between the χ^2 value that encloses 68% (or 95% or 99%) of the simulations and the minimum χ^2 value at this $z_{\rm phot}$. Next, we return to the full χ^2 grid that resulted from FAST. The confidence intervals for a given parameter are the minimum and maximum values in the full model cube with a χ^2 value less than $\chi^2_{\rm min} + \Delta\chi^2$ *and* a redshift within the 68% confidence interval as provided by EAZY. In essence, we use the EAZY output to limit the redshift range of the solutions allowed in FAST. Note that $\chi^2_{\rm min}$ of the full grid is likely lower than the minimum value of χ^2 at $z_{\rm phot}$. We tested this method using a large number of Monte Carlo simulations that are input in both EAZY and FAST (retaining the combinations of $z_{\rm phot}$ and perturbed fluxes). In this case we do not use the simulations for calibration, but derive the uncertainties directly from the output. We find good correlations between the uncertainties of the two methods and we believe that the FAST confidence levels are robust and reliable.

REFERENCES

Balogh, M. L., Morris, S. L., Yee, H. K. C., Carlberg, R. G., & Ellingson, E. 1999, ApJ, 527, 54
Bezanson, R., van Dokkum, P. G., Tal, T., Marchesini, D., Kriek, M., Franx, M., & Coppi, P. 2009, ApJ, 697, 1290

Bower, R. G., et al. 2006, MNRAS, 370, 645
Brammer, G., & van Dokkum, P. G. 2007, ApJ, 654, L107
Brammer, G., van Dokkum, P. G., & Coppi, P. 2008, ApJ, 686, 1503
Bruzual, G., & Charlot, S. 2003, MNRAS, 344, 1000
Calzetti, D., Armus, L., Bohlin, R. C., Kinney, A. L., Koornneef, J., & Storchi-Bergmann, T. 2000, ApJ, 533, 682
Chabrier, G. 2003, PASP, 115, 763
Chapman, S. C., Smail, I., Blain, A. W., & Ivison, R. J. 2004, ApJ, 614, 671
Cimatti, A., et al. 2008, A&A, 482, 21
Conroy, C., Gunn, J. E., & White, M. 2009, ApJ, submitted (arXiv:0809.4261)
Croton, D. J., et al. 2006, MNRAS, 365, 11
Daddi, E., et al. 2004a, ApJ, 600, L127
Daddi, E., et al. 2004b, ApJ, 617, 746
Daddi, E., et al. 2005, ApJ, 626, 680
Damen, M., Labbé, I., Franx, M., van Dokkum, P. G., Taylor, E. N., & Gawiser, E. J. 2009, ApJ, 690, 937
Damjanov, I., et al. 2009, ApJ, 695, 101
Davé, R. 2008, MNRAS, 385, 147
Dekel, A., & Birnboim, Y. 2008, MNRAS, 383, 119
Dopita, M. A., & Sutherland, R. S. 1995, ApJ, 455, 468
Elias, J. H., et al. 2006, Proc. SPIE, 6269, 139
Fontana, A., et al. 2009, A&A, in press (arXiv:0901.2898)
Förster Schreiber, N. M., et al. 2004, ApJ, 616, 40
Franx, M., van Dokkum, P. G., Förster Schreiber, N. M., Wuyts, S., Labbé, I., & Toft, S. 2008, ApJ, 688, 770
Franx, M., et al. 2003, ApJ, 587, L79
Gawiser, E., et al. 2006, ApJS, 162, 1
Greene, J. E., & Ho, L. C. 2005, ApJ, 627, 721
Heckman, T. M. 1980, A&A, 87, 152
Hopkins, P. F., Cox, T. J., Kereš, D., & Hernquist, L. 2008, ApJS, 175, 390
Hopkins, P. F., Bundy, K., Murray, N., Quataert, E., Lauer, T., & Ma, C.-P. 2009b, MNRAS, submitted (arXiv:0903.2479)
Hopkins, P. F., Lauer, T. R., Cox, T. J., Hernquist, L., & Kormendy, J. 2009a, ApJS, 181, 486
Kannappan, S. J., & Gawiser, E. 2007, ApJ, 657, L5
Kennicutt, R. C. 1998, ARA&A, 36, 189
Kewley, L. J., & Dopita, M. A. 2002, ApJS, 142, 35
Kewley, L. J., Dopita, M. A., Sutherland, R. S., Heisler, C. A., & Trevena, J. 2001, ApJ, 556, 121
Kriek, M., et al. 2006a, ApJ, 645, 44
Kriek, M., et al. 2006b, ApJ, 649, L71
Kriek, M., et al. 2007, ApJ, 669, 776
Kriek, M., van der Wel, A., van Dokkum, P. G., Franx, M., & Illingworth, G. D. 2008b, ApJ, 682, 896
Kriek, M., et al. 2008a, ApJ, 677, 219
Kroupa, P. 2001, MNRAS, 322, 231
Labbé, I., et al. 2003, AJ, 125, 1107
Labbé, I., et al. 2005, ApJ, 624, L81
Longhetti, M., et al. 2007, MNRAS, 274, 614
Mancini, C., et al. 2009, A&A, in press (arXiv:0901.3341)
Maraston, C. 2005, MNRAS, 362, 799
Marchesini, D., van Dokkum, P. G., Förster Schreiber, N. M., Franx, M., Labbé, I., & Wuyt, S. 2009, ApJ, submitted (arXiv:0811.1773)
Mobasher, B., et al. 2005, ApJ, 635, 832
Moustakas, J., Kennicutt, R. C., & Tremonti, C. A. 2006, ApJ, 642, 775
Muzzin, A., Marchesini, D., van Dokkum, P. G., Labbé, I., Kriek, M., & Franx, M. 2009, ApJ, submitted
Naab, T., Johansson, P. H., & Ostriker, J. P. 2009, ApJ, submitted
Naab, T., Johansson, P. H., Ostriker, J. P., & Efstathiou, G. 2007, ApJ, 658, 710
Quadri, R., et al. 2007, AJ, 134, 1103
Reddy, N. A., et al. 2006, ApJ, 644, 792
Salpeter, E. E. 1955, ApJ, 121, 161
Saracco, P., Longhetti, M., & Andreon, S. 2009, MNRAS, 392, 718
Shapley, A. E., Steidel, C. C., Adelberger, K. L., Dickinson, M., Giavalisco, M., & Pettini, M. 2001, ApJ, 562, 95
Shapley, A. E., et al. 2005, ApJ, 626, 698
Shields, G. A. 1990, ARA&A, 28, 525
Tacconi, L. J., et al. 2008, ApJ, 680, 246
Taylor, E. N., et al. 2009a, ApJ, 694, 1171
Taylor, E. N., et al. 2009b, ApJ, submitted (arXiv:0903.3051)
Toft, S., et al. 2007, ApJ, 671, 285
Trujillo, I., Conselice, C. J., Bundy, K., Cooper, M. C., Eisenhardt, P., & Ellis, R. S. 2007, MNRAS, 382, 109
Trujillo, I., et al. 2006, ApJ, 650, 18
van der Wel, A., Holden, B. P., Zirm, A. W., Franx, M., Rettura, A., Illingworth, G. D., & Ford, H. C. 2008, ApJ, 688, 48

---

[9] Note that we did not apply this method in Kriek et al. ([2008b](#)); instead, we arbitrarily increased the uncertainties by quadratically adding 10% of the average flux of the spectrum to account for systematic effects.

van der Wel, A., van den Bell, E. F., Bosch, F. C., Gallazzi, A., & Rix, H.-W. 2009, ApJ, in press (arXiv:0903.4857)

van Dokkum, P. G., et al. 2004, ApJ, 611, 703

van Dokkum, P. G., et al. 2006, ApJ, 638, L59

van Dokkum, P. G., et al. 2008, ApJ, 677, L5

Wall, J. V., Pope, A., & Scott, D. 2008, MNRAS, 383, 435

Wiklind, T., Dickinson, M., Ferguson, H. C., Giavalisco, M., Mobasher, B., Grogin, N. A., & Panagia, N. 2008, ApJ, 676, 781

Williams, R. J., Quadri, R. F., Franx, M., van Dokkum, P. G., & Labbé, I. 2008, ApJ, 691, 1879

Wuyts, S., et al. 2007, ApJ, 655, 51

Zirm, A. W., et al. 2007, ApJ, 656, 66